



An iterative image reconstruction algorithm combined with forward and backward diffusion filtering for in-line X-ray phase-contrast computed tomography

Yuqing Zhao,^a Mengyu Sun,^a Dongjiang Ji,^b Changhong Cong,^c Wenjuan Lv,^a Qi Zhao,^a Lili Qin,^a Jianbo Jian,^d Xiaodong Chen^e and Chunhong Hu^{a*}

Received 16 November 2017

Accepted 26 June 2018

Edited by A. Momose, Tohoku University, Japan

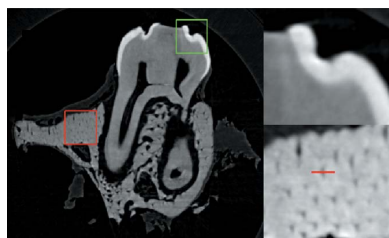
Keywords: in-line X-ray phase-contrast computed tomography; simultaneous algebraic reconstruction technique; forward and backward diffusion filtering; few-view projections.

^aCollege of Biomedical Engineering, Tianjin Medical University, Tianjin 300070, People's Republic of China, ^bThe School of Science, Tianjin University of Technology and Education, Tianjin 300222, People's Republic of China, ^cThe Dental Hospital of Tianjin Medical University, Tianjin 300070, People's Republic of China, ^dRadiation Oncology Department, Tianjin Medical University General Hospital, Tianjin 300070, People's Republic of China, and ^eKey Laboratory of Opto-electronic Information Technology, Ministry of Education (Tianjin University), Tianjin 300072, People's Republic of China. *Correspondence e-mail: chunhong_hu@hotmail.com

In-line X-ray phase-contrast computed tomography (IL-PCCT) can reveal fine inner structures for low-*Z* materials (*e.g.* biological soft tissues), and shows high potential to become clinically applicable. Typically, IL-PCCT utilizes filtered back-projection (FBP) as the standard reconstruction algorithm. However, the FBP algorithm requires a large amount of projection data, and subsequently a large radiation dose is needed to reconstruct a high-quality image, which hampers its clinical application in IL-PCCT. In this study, an iterative reconstruction algorithm for IL-PCCT was proposed by combining the simultaneous algebraic reconstruction technique (SART) with eight-neighbour forward and backward (FAB8) diffusion filtering, and the reconstruction was performed using the Shepp–Logan phantom simulation and a real synchrotron IL-PCCT experiment. The results showed that the proposed algorithm was able to produce high-quality computed tomography images from few-view projections while improving the convergence rate of the computed tomography reconstruction, indicating that the proposed algorithm is an effective method of dose reduction for IL-PCCT.

1. Introduction

X-ray phase-contrast imaging (PCI) is a powerful imaging technique that can detect subtle differences in the electron density of materials or tissues. Regardless of the anisotropy in the medium, the refractive index, *n*, which characterizes the optical properties of an object, can be described with its complex form: $n = 1 - \delta + i\beta$, where δ is the refractive index decrement responsible for the phase information; however, the imaginary part, β , is the attenuation coefficient of the X-ray beam passing through the object responsible for the absorption information (Chen *et al.*, 2013). For weakly absorbing objects such as biological soft tissues, phase information plays a more important role than the absorption information, because δ is approximately three orders of magnitude higher than β (Momose *et al.*, 1996; Stampanoni *et al.*, 2011; Brandlhuber *et al.*, 2016). Compared with conventional absorption-based X-ray imaging, phase-based PCI enables the acquisition of images with higher resolution in biological soft tissues. As a result, PCI has been particularly applied to visualize soft tissue details and has become one of the most popular pre-clinical imaging techniques (Bravin & Coan, 2012).



In the past decade, various PCI techniques have been proposed; the four major types are X-ray interferometry, diffraction-enhanced imaging (DEI), X-ray grating interferometry and in-line X-ray phase-contrast imaging (IL-PCI). Among these methods, IL-PCI shows a high potential to become clinically applicable because of its simplicity (Lee, 2015). By extending IL-PCI to computed tomography (CT), in-line X-ray phase-contrast computed tomography (IL-PCCT) holds outstanding potential to reveal detailed microstructures inside biological tissues at micrometre-scale resolution (Liu *et al.*, 2010; Xuan *et al.*, 2015; Hetterich *et al.*, 2016; Cao *et al.*, 2017). Typically, filtered back-projection (FBP) is utilized to reconstruct CT images in IL-PCCT. However, to produce high-quality images, the FBP algorithm requires many projections, which leads to a large total exposure time and thus a large radiation dose. It is significant for clinical applications of IL-PCCT to reduce the radiation dose while maintaining the high quality of reconstructed images. In IL-PCCT, one approach to decrease the radiation dose is to shorten the total exposure time by reducing the number of projections, such as few-view projections (Melli *et al.*, 2016). The CT iterative reconstruction algorithm can provide excellent reconstructed results from few-view projections and thus has a high potential for IL-PCCT. The simultaneous algebraic reconstruction technique (SART) is an important algebraic iterative reconstruction method (Hansen & Saxild-Hansen, 2012) that formulates the reconstruction problem as a discrete linear transformation and can reconstruct better results than the FBP algorithm using few-view projections. However, when applying the SART algorithm in the case of few-view projections, the reconstructed images still retain some artefacts (*e.g.* streak artefacts, oscillating artefacts, *etc.*), which suggests that the performance of the SART algorithm still needs to be improved.

The current strategies of few-view CT reconstruction assume that the reconstructed images are piecewise smooth and include the design of regularization techniques for detail preserving and artefact smoothing in the CT reconstruction procedure, such as the total variation (TV) regularization approach (Sidky *et al.*, 2006). These regularization-based CT reconstruction techniques typically sacrifice regional fine textures and may compromise clinical tasks. Notably, many IL-PCCT images of biological tissues containing complex textures cannot satisfy the assumption of piecewise smoothness, and the regularization techniques developed under this assumption may have limited ability to address this case. To overcome the limitation from the above-mentioned assumption, one possible framework for few-view IL-PCCT reconstruction is to incorporate an anisotropic filtering method, based on local image features, into the CT iterative reconstruction procedure. In 2002, Gilboa *et al.* proposed a forward and backward (FAB) diffusion-filtering method (Gilboa *et al.*, 2002). As a powerful nonlinear anisotropic diffusion filtering method, the FAB method can adaptively control diffusion filtering force based on gradient information of local features in the image, thereby enabling a synergy of artefact smoothing and detail preserving. To date, due to its excellent performance in detail

preserving and denoising, the FAB method has been developed and applied in many types of images, including synthetic aperture radar images (Zhou *et al.*, 2004), ultrasound images (Nieniewski, 2014) and magnetic resonance images (Prasath *et al.*, 2015). To the best of our knowledge, no study has shown that the FAB method can be used in IL-PCCT images. Hence, the FAB method was employed here to preserve detailed features and smooth artefacts in the IL-PCCT reconstruction procedure. As gradients of eight neighbours were able to represent the more accurate local features of the image, we developed an eight-neighbour FAB algorithm (FAB8).

In this study, the FAB8 method and the SART algorithm were combined to develop CT reconstruction, and a SART-FAB8 algorithm was proposed and applied in IL-PCCT reconstructions with few-view projection data. The proposed method consists of two steps per iteration. First, the SART-step is performed to enforce consistency of the inconsistent projection data and acquire the reconstructed image with artefacts. Second, the FAB step is utilized to reduce the artefacts in the reconstruction image acquired from the ‘SART step’ and improve the convergence of image reconstruction. Finally, the Shepp–Logan phantom simulation and synchrotron IL-PCCT experiment were performed to demonstrate the effectiveness and ability of the proposed algorithm.

2. Methods

2.1. IL-PCI and its phase retrieval

As a propagation-based imaging technique, IL-PCI (Snigirev *et al.*, 1995) can produce high-resolution images in weakly absorbing materials, especially for biological tissues (Rastogi *et al.*, 2013; Jian *et al.*, 2016; Mai *et al.*, 2017). In IL-PCI, when the quasi-coherent X-ray beams illuminate the object they will yield the spatially varying phase shifts in the X-ray beams. As the beams propagate from the object, the distorted wavefront, which has undergone different deflections, will generate a characteristic pattern in the image plane. Due to Fresnel diffraction, the phase shifts are subsequently transformed to detectable intensity variations, and finally recorded by the detector. In practice, IL-PCI presents a very simple experimental setup for PCI (see Fig. 1). IL-PCI requires no additional optical element compared with the conventional CT modality except that the provided X-ray beams are sufficiently spatially coherent and the sample-to-detector distance (SDD) is variable (Chen *et al.*, 2012). Due to its high resolution in biological tissues and simplicity of experimental setup, IL-PCI has been widely used in biological science and is one of the most important pre-clinical imaging techniques.

However, projection images from IL-PCI contain absorption information and phase information (Chen *et al.*, 2011) and, therefore, phase retrieval may be implemented to extract the phase information. Generally, phase retrieval requires at least two phase-contrast radiographs, taken at two different SDDs (Nugent *et al.*, 1996), but this method delivers a high

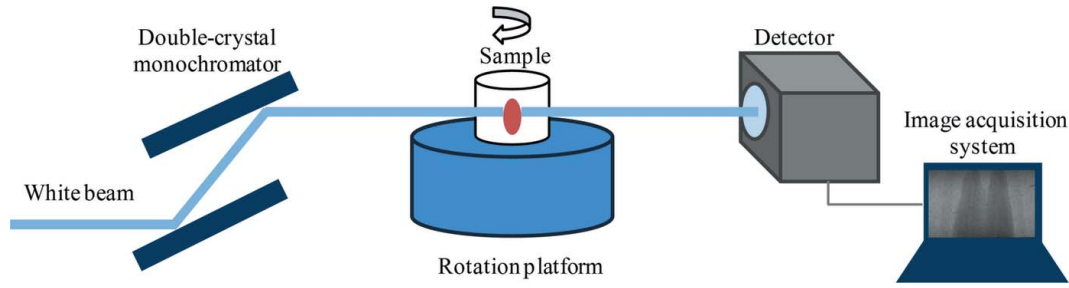


Figure 1

Schematic depiction of the IL-PCI setup at BL13W at Shanghai Synchrotron Radiation Facility (SSRF). Here, a white beam was monochromated by a double-crystal monochromator, and the sample was illuminated on the rotation platform. When the transmitted beam passed through the sample, the density variation resulted in phase shifts. Finally, a projection image, containing a mix of phase shifts and attenuation coefficients, could be recorded by the detector in the image plane and subsequently displayed in the image acquisition system. For tomographic scans, the sample can be rotated from 0° to 180° to acquire the projection images from various views.

radiation dose to the samples and encounters a complicated registration problem. According to Gureyev’s study, phase retrieval from a single SDD IL-PCCT data set is possible (Gureyev *et al.*, 2004), and several phase-retrieval methods using single SDD IL-PCCT data have been proposed, *e.g.* the Modified Bronnikov algorithm (MBA) method (Bronnikov, 1999, 2002; Groso *et al.*, 2006), the TIE-based method by Paganin (Paganin *et al.*, 2002; Wu *et al.*, 2005), and the phase-attenuation duality Bronnikov algorithm (PAD-BA) (Chen *et al.*, 2013). In this study, PAD-BA, a single SDD phase-retrieval method, was implemented on projection images using *PITRE* software to extract quantitative phase information (Chen *et al.*, 2012). This algorithm is grounded in *a priori* knowledge that the δ and β parts of the complex refractive index are proportional to each other. In our experiment, by some experimental trials, we found that the reconstructed image using a δ/β value of 1000 has a high contrast between the adjoining tissues and enables an optimal distinguishing performance in the regions of edge details and fine textures, which is the best result for our subsequent research, and thus 1000 was considered as the best δ/β value. After phase retrieval, the phase information distribution from the IL-PCI of samples can be obtained and its quantitative analysis can be performed.

2.2. The CT iterative reconstruction method

In the IL-PCCT experiment, the imaging model can be approximated to a discrete linear transformation as follows,

$$p = Af, \quad (1)$$

where A stands for an $M \times N$ system matrix that represents the X-ray parallel beam forward projection, $p \in R^M$ is the projection data acquired from the detector, and $f \in R^N$ denotes the phase information distribution of the illuminated object. The goal of IL-PCCT reconstruction is to accurately reconstruct f from p .

In this work, a block-iterative based SART technique is adopted, which has the potential to handle large-scale data quickly, and is expressed as follows,

$$f^{(k+1)} = f^{(k)} + \lambda_k V^{-1} A^T W(p - Af^{(k)}), \quad (2)$$

where k is the number of iterations, λ_k represents the relaxation coefficient of the k th iteration, T stands for the transpose operator, and V and W are the diagonal matrixes with row sums and column sums of A in the diagonal, respectively.

To improve the convergence performance of the SART algorithm, λ_k is chosen using the line search method (Hansen & Saxild-Hansen, 2012), which can be computed as follows,

$$\lambda_k = (p - Af^{(k)})^T W(p - Af^{(k)}) / \|A^T(p - Af^{(k)})\|_2^2, \quad (3)$$

where $\|\dots\|_2^2$ represents the square of the nuclear norm.

2.3. The FAB method

The FAB method contains forward diffusion and backward diffusion processes, and it is able to switch the diffusion process between the forward diffusion and backward diffusion according to the diffusion coefficient (*i.e.* when the diffusion coefficient is positive, it is the forward diffusion process; when negative, it is the backward diffusion process). The forward diffusion process is capable of smoothing low gradients and thus enables suppression of the streak artefacts and oscillating artefacts in the image. Backward diffusion can retain local high gradients and thus enables preservation of edge details and fine textures in the image. The diffusion coefficient can be locally adjusted *via* image features (*e.g.* edges, textures and moments). Thus, the FAB method enables adaptive control of forward diffusion and backward diffusion processes based on the local features in the image. The formulation of FAB is defined as follows,

$$\begin{aligned} \frac{\partial f(i, j, t)}{\partial t} &= \text{div}[c(|\nabla f|) \nabla f], \\ f(i, j, 0) &= f_0(i, j), \\ c(|\nabla f|) &= \frac{1}{1 + (|\nabla f|/k_t)^n} - \frac{\alpha}{1 + [(|\nabla f| - k_b)/\omega]^{2m}}, \end{aligned} \quad (4)$$

where (i, j) denotes the coordinates of a pixel in the 2D image domain, t represents the evolution time (iterations), $\text{div}[\dots]$ is the diffusion operator, $c(\dots)$ is the diffusion coefficient,

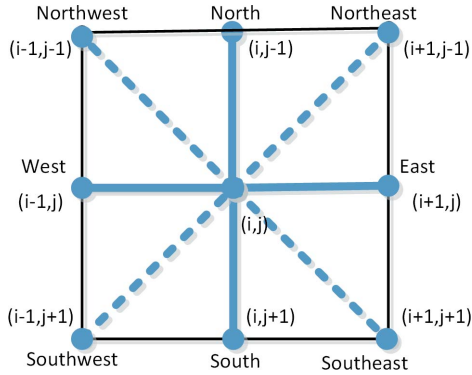

Figure 2

Illustration of gradients of eight neighbours. Blue solid lines represent gradients of four neighbours, and blue solid lines and blue dotted lines on the diagonal represent gradients of eight neighbours. Here, east (E), west (W), south (S), north (N), southeast (SE), southwest (SW), northeast (NE) and northwest (NW) denote eight directions.

f_0 represents the image f at the initial time, and ∇f is the gradient of the image f . The parameter k_f is the maximum value in the forward diffusion process, and it controls the gradient magnitudes for forward diffusion. The parameters k_b and ω define the centre and width of the backward diffusion process, respectively. The parameter α determines the ratio between the strength of the forward and backward forces. In addition, m and n are the exponent parameters for the forward force and backward force, respectively.

To improve the performance of FAB, we developed the FAB8 method to replace the original four-neighbour FAB (FAB4). Here, let $\nabla f_{i,j}^d$, and $d = E, W, S, N, SE, SW, NE, NW$ define the gradients of eight neighbours in eight directions (see Fig. 2), and the definitions are expressed as follows,

$$\begin{aligned}
 \nabla f_{i,j}^E &= f_{i+1,j} - f_{i,j}, \\
 \nabla f_{i,j}^W &= f_{i-1,j} - f_{i,j}, \\
 \nabla f_{i,j}^S &= f_{i,j+1} - f_{i,j}, \\
 \nabla f_{i,j}^N &= f_{i,j-1} - f_{i,j}, \\
 \nabla f_{i,j}^{SE} &= f_{i+1,j+1} - f_{i,j}, \\
 \nabla f_{i,j}^{SW} &= f_{i-1,j+1} - f_{i,j}, \\
 \nabla f_{i,j}^{NE} &= f_{i+1,j-1} - f_{i,j}, \\
 \nabla f_{i,j}^{NW} &= f_{i-1,j-1} - f_{i,j}.
 \end{aligned} \tag{5}$$

Let $c_{i,j}^{\text{center}}$ define the diffusion coefficient of the central difference of the image f in some pixel (i, j) , and $c_{i,j}^d$, $d = E, W, S, N, SE, SW, NE, NW$ define the diffusion coefficients of the gradients of eight neighbours in eight directions, which are formulated as follows,

$$c_{i,j}^{\text{center}} = c \left(\left| \frac{f_{i+1,j} - f_{i-1,j}}{2} \right|^2 + \left| \frac{f_{i,j+1} - f_{i,j-1}}{2} \right|^2 \right)^{1/2}, \tag{6}$$

$$c_{i,j}^d = c(|\nabla f_{i,j}^d|). \tag{7}$$

To improve the computational stability of FAB in space-discrete diffusion form, a modified space-discrete FAB diffu-

sion of the framework of Weik *et al.* (2009) was adopted, and the fluxes can be expressed as follows,

$$\Phi_{i,j}^d = \left(\frac{c_{i,j}^d + c_{i,j}^{\text{center}}}{2} \right) \nabla f_{i,j}^d. \tag{8}$$

The continuous nonlinear diffusion in equation (4) can be discretely presented *via* eight nearest neighbours and the discrete partial differential equations (PDEs) solution (Gerig *et al.*, 1992) can be formulated as follows,

$$\begin{aligned}
 f^t &= f^{t-1} + \Delta t (\Phi^E - \Phi^W + \Phi^S - \Phi^N \\
 &\quad + \Phi^{SE} - \Phi^{SW} + \Phi^{NE} - \Phi^{NW}),
 \end{aligned} \tag{9}$$

where Δt is the time step that ranges from 0 to 0.25, and f^t denotes the updated image of the t th iteration in the FAB diffusion process.

2.4. Pseudocode for SART-FAB8 algorithm

By combining the FAB8 method with the SART reconstruction, we developed the SART-FAB8 algorithm for IL-PCCT. In summary, the pseudocode of the SART-FAB8 algorithm was presented as follows.

Algorithm 1. Pseudocode for SART-FAB8 algorithm.

Input: projection data p , initialized image $f_{SART}^0 = \text{zeros}(m \times m, 1)$, the total iteration number k_{max} , the iteration number of the FAB kk_{max} , the time step Δt , the exponent parameters m and n .

- 1: **While** $i \leq k_{\text{max}}$ **do**
 - 2: $\lambda_i = (p - Af_{SART}^{(i)})^T W (p - Af_{SART}^{(i)}) / \|A^T (p - Af_{SART}^{(i)})\|_2^2$;
 - 3: $f_{SART}^{(i)} = f_{SART}^{(i-1)} + \lambda_i V^{-1} A^T W (p - Af_{SART}^{(i-1)})$;
 - 4: $f_{SART}^{(i)} (f_{SART}^{(i)} < 0) = 0$; % nonnegative constraint
 - 5: $f_{SART}^{(i+1)} = \text{reshape}(f_{SART}^{(i)}, m, m)$;
 - 6: **for** $j = 1 : kk_{\text{max}}$
 - 7: Calculate MAG and obtain the parameters:
 $k_f = 1 \times \text{MAG}$, $k_b = 1.6 \times \text{MAG}$, $\omega = 0.5 \times \text{MAG}$, $\alpha = k_f / 4(k_b + \omega)$.
 - 8: % $f_{SART-FAB8}^{(j)} = f_{SART-FAB8}^{(j-1)} + \Delta t (\Phi^E - \Phi^W + \Phi^S - \Phi^N + \Phi^{SE} - \Phi^{SW} + \Phi^{NE} - \Phi^{NW})$;
 $\% f_{SART-FAB4}^{(j)} = f_{SART-FAB4}^{(j-1)} + \Delta t (\Phi^E - \Phi^W + \Phi^S - \Phi^N)$;
 - 9: **end for**
 - 10: $f_{SART}^{(i+1)} = \text{reshape}(f_{SART-FAB8}^{(kk_{\text{max}})}, m \times m, 1)$;
 - 11: **end while**
 - 12: $f_{SART-FAB8} = \text{reshape}(f_{SART}^{(k_{\text{max}})}, m, m)$;
- Output:** $f_{SART-FAB8}$.
-

2.5. Low-dose noise model in projections for the simulation

To analyze the robustness to low-dose noise of the proposed algorithm, the low-dose noise was introduced into the projection data and the corresponding image reconstructions were performed. Inspired by the previous work (Liu *et al.*, 2012; Bian *et al.*, 2017), the low-dose noise in projections can be modelled as a combination of the Poisson-distributed

photon noise and Gaussian-distributed electronic noise, as shown in equation (10),

$$\tilde{I}_i = \text{Poisson}[I_0 \exp(-\tilde{y}_i)] + \text{Gaussian}(m_{ie}, \sigma_{ie}^2), \quad (10)$$

where \tilde{I}_i is the simulated noisy measurement for detector element i at a projection view and I_0 represents the incident X-ray intensity, \tilde{y}_i is the logarithmic transform of \tilde{I}_i , m_{ie} and σ_{ie}^2 are the mean and variance of the background electronic noise, for detector element i . In this study, the X-ray exposure level I_0 was set to 1.0×10^5 , and m_{ie} and σ_{ie}^2 were set to 0 and 10, respectively, for low-dose noisy projections simulation.

2.6. Parameter selection for the SART-FAB algorithm

The backward diffusion process is considered as an ill-posed problem due to its computational instability. To tackle the ill-posed problem in FAB, Gilboa *et al.* (2002) showed that three conditions should be fulfilled, and these conditions are formulated as follows,

(i)

$$\max_{|\nabla f| < k_f} \{|\nabla f| c(|\nabla f|)\} > \max_{k_b - \omega < |\nabla f| < k_b + \omega} \{|\nabla f| c(|\nabla f|)\};$$

(ii)

$$k_f \leq k_b - \omega, \quad \text{for any } 0 < \omega < k_b - k_f;$$

(iii)

$$\alpha \leq k_f/2(k_b + \omega), \quad \text{for any } 0 < \omega < k_b - k_f.$$

In this study, the mean absolute gradient (MAG) is implemented to adaptively tune the parameters in FAB according to local gradient information for the image. However, the performance of the FAB method also depends on constant coefficients in MAG-based parameters, such as k_f , k_b , ω and α . As for the selection of constant coefficients in MAG-based parameters in the most general case, generally, when being adopted to reconstruct some objects with much noise, considering that the parameter k_f stands for the strength of smoothing force, a larger coefficient in parameter k_f would have a better denoising effect; when being adopted to reconstruct some objects with fine edge details and textures, considering that the parameters k_b and ω control the range of preservation of edge details and fine textures, a larger coefficient in parameter k_b would guarantee clearer edge details and textures; as for the balance parameter α , which is the ratio between the the strength of forward diffusion and backward diffusion, it can be tuned according to actual needs. Since an optimal set of constant coefficients in MAG-based parameters will enable the best performance of FAB and, inspired by previous work (Tsiotsios & Petrou, 2012; Yang *et al.*, 2015), on the basis of satisfaction of the above three conditions, the optimal constant coefficients can be found in the following way. First, the constant coefficient of one parameter was continuously changed using different scales while fixing the other parameters to generate different image reconstructions. Second, the errors between the above reconstructed results and the reference image were calculated, *i.e.* the root mean

squared error. Finally, the optimal constant coefficient can be determined using the minimal reconstructed error. The other optimal coefficients and parameters can also be found using this method. After trial and error, we obtained the best performance for the cases with and without noise using the following two sets of parameters: (i) one set for the case without noise: $kk_{\max} = 10$, $k_f = 1 \times \text{MAG}$, $k_b = 1.6 \times \text{MAG}$, $\omega = 0.5 \times \text{MAG}$, $\alpha = k_f/4(k_b + \omega)$, $n = 4$, $m = 2$, $\Delta t = 0.15$; (ii) the other set for the case with the low-dose noise: $kk_{\max} = 10$, $k_f = 1.4 \times \text{MAG}$, $k_b = 2.4 \times \text{MAG}$, $\omega = 0.8 \times \text{MAG}$, $\alpha = k_f/3(k_b + \omega)$, $n = 4$, $m = 2$, $\Delta t = 0.15$. In general, the first set of parameters can be used to reconstruct many objects from the noise-free projections, including some simulations and practical applications; in this work, these parameters were used for the simulation in the noise-free case and practical experiment. For the simulation in the low-dose noise case, the second set of parameters were adopted. Although the above two sets of parameters cannot fit to all objects, the optimal parameters for the other reconstructed object can also be determined in the above-mentioned way.

2.7. Quantitative assessment of the reconstructed images

Three quantitative metrics, including universal quality index (UQI), peak signal-to-noise ratio (PSNR) and root mean squared error (RMSE), are adopted to quantitatively assess the quality of reconstructed images. The UQI can be used to evaluate the pixel-to-pixel similarity between a reconstructed and reference image, which yields a value between 0 and 1 that increases with increasing similarity (Wang & Bovik, 2002). PSNR is a traditional measure of image quality, and a larger value indicates better quality. RMSE is used to evaluate the reconstruction accuracy based on error sensitivity, and a smaller value means more accuracy.

(i) UQI is widely used and defined as follows,

$$\text{UQI}(x, y) = \frac{2 \text{Cov}(x, y)}{(\sigma_x^2 + \sigma_y^2)} \frac{2u_x u_y}{(u_x^2 + u_y^2)}, \quad (11)$$

where x is the reference image, y is the reconstructed image and u_x and u_y are the means of x and y , respectively; σ_x^2 and σ_y^2 denote the variances of x and y , respectively; and $\text{Cov}(x, y)$ is the covariance between x and y .

(ii) PSNR is defined as follows,

$$\text{MSE}(x, y) = \frac{1}{M \times N} \sum_{i=1}^M \sum_{j=1}^N (x_{i,j} - y_{i,j})^2, \quad (12)$$

$$\text{PSNR}(x, y) = 10 \log_{10} \left(\frac{\text{Peak}^2}{\text{MSE}} \right), \quad (13)$$

where MSE is the mean square error function, and the size of the reconstructed and the reference images are $M \times N$; $x_{i,j}$ represents the pixel intensity of the reference image in some pixel (i, j) , $y_{i,j}$ represents the pixel intensity of the reference image in some pixel (i, j) ; and Peak is the largest pixel value in the normalized image, *e.g.* in the case of eight-bit pixel representation it is 255.

(iii) RMSE is defined as follows,

$$\text{RMSE}(x, y) = \left[\frac{1}{M \times N} \sum_{i=1}^M \sum_{j=1}^N (x_{i,j} - y_{i,j})^2 \right]^{1/2}. \quad (14)$$

3. Simulation experiment

3.1. Simulations

To evaluate the performance of the SART-FAB8 algorithm, the standard Sheep–Logan phantom was utilized (Fig. 3*a*). In this experiment, semi-circular angle scanning based on parallel-beam geometry was used to simulate the process of IL-PCI, and a Sheep–Logan phantom image with a matrix size of 512×512 pixels was used to simulate the phase information distribution of the sample (Langer *et al.*, 2009; Yang *et al.*, 2015). The detector is modelled as a straight-line array with 724 elements, and the size of the reconstructed images is 512×512 pixels. The 60 uniformly distributed projections without noise and with noise over π -view were used to simulate few-view projections and low-dose noisy few-view projections, respectively; the low-dose noise added into few-view projections was introduced in detail in §2.5. Here, in order to reduce the effects from the FBP sampling errors, the missing 300-view projections were compensated by interpolation between the acquired 60-view projections, and then the compensated projections were used for the FBP. As the stopping criterion, the total iteration number of 20 was selected for SART, SART-FAB4 and SART-FAB8 algorithms according to the convergence curves, as shown in Fig. 6. Here, the FBP, SART and SART-FAB4 algorithms were used for comparison with the SART-FAB8 algorithm, and all parameters were optimally chosen for the best performance, which were introduced in detail in §2.6. All experiments were conducted using the MATLAB programming language on a desktop PC platform equipped with Intel(R) Core(TM) i5-4460 CPU at 3.2 GHz and 16 GB RAM.

3.2. Experimental results

Four images from 60-view noise-free projections and four images from 60-view noisy projections were reconstructed

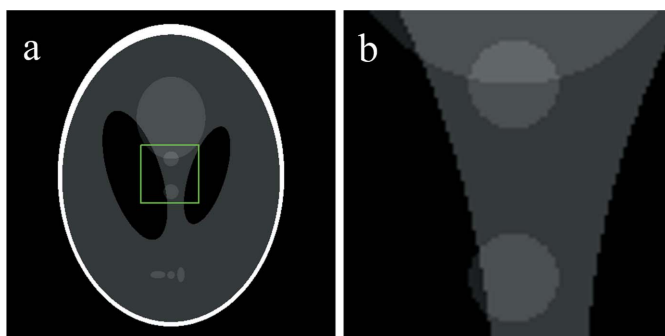


Figure 3 Phantom used for evaluating CT reconstruction algorithms. (a) True Shepp–Logan phantom image. (b) Magnified image of the green rectangle regions in (a).

Table 1

Quality metrics for the reconstructed Sheep–Logan images in Fig. 4.

	Method	UQI	PSNR (dB)	RMSE	Time (s)
Noise-free	FBP	0.9053	21.7293	0.3320	0.3120
	SART	0.9363	23.7194	0.2216	77.5998
	SART-FAB4	0.9577	26.8583	0.1215	93.4211
	SART-FAB8	0.9790	27.3615	0.1023	107.6200
Noise-added	FBP	0.8790	20.7825	0.3702	0.4836
	SART	0.9032	22.5036	0.3298	144.8783
	SART-FAB4	0.9476	24.2517	0.2201	182.2993
	SART-FAB8	0.9663	25.7206	0.2032	206.4626

using FBP, SART, SART-FAB4 and SART-FAB8 algorithms, as shown in Figs. 4(*a*)–4(*d*) and 4(*i*)–4(*l*). Among the reconstructed images, the images reconstructed using the FBP algorithm are worst, and are seriously affected by a large number of streak artefacts and low-dose noise, indicating that the FBP algorithm has a poor ability to deal with few-view projection data for the cases with and without noise [Figs. 4(*a*) and 4(*i*)]. The images reconstructed using the SART algorithm are better than those of the FBP algorithm, where the streak artefacts and low-dose noise are effectively reduced. However, the edges and textures of the image are affected by the low-dose noise and oscillating artefacts due to the loss of high-frequency information in the few-view projections [Figs. 4(*b*) and 4(*j*)]. The reconstructed images of the SART-FAB4 [Figs. 4(*c*) and 4(*k*)] and SART-FAB8 [Figs. 4(*d*) and 4(*l*)] algorithms are better than those using the FBP and SART algorithms, where the streak artefacts, oscillating artefacts and low-dose noise are effectively reduced, implying that the SART-FAB4 and SART-FAB8 algorithms can suppress streak artefacts, oscillating artefacts and low-dose noise. Nevertheless, in contrast with SART-FAB4, the reconstructed images of SART-FAB8 have clearer edges and are closer to the true image.

3.3. Assessments

To compare the accuracy of the four reconstruction algorithms, horizontal profiles of the same position in Figs. 4(*a*)–4(*d*) and Figs. 4(*i*)–4(*l*) are utilized, as shown in Fig. 5. It is easy to see that the profiles of the SART-FAB8 algorithm are closest to the true result in the cases with and without noise. Additionally, the UQI, PSNR and RMSE values of the reconstructed images were further calculated, and the computation times of the four reconstruction algorithms were also computed, as shown in Table 1. As seen from Table 1, the computation times of the SART-FAB8 algorithm are longest in the cases with and without noise; however, the quality of the images reconstructed using the SART-FAB8 algorithm is obviously the best.

To qualitatively evaluate the convergence performance of the SART, SART-FAB4 and SART-FAB8 algorithms in the cases with and without noise, the RMSE-based convergence curves of the above-mentioned methods are presented (Fig. 6). As seen in Fig. 6, the SART, SART-FAB4 and SART-FAB8 algorithms converged before the iterations reach 20, with the convergence rate of the SART-FAB8 algorithm being fastest.

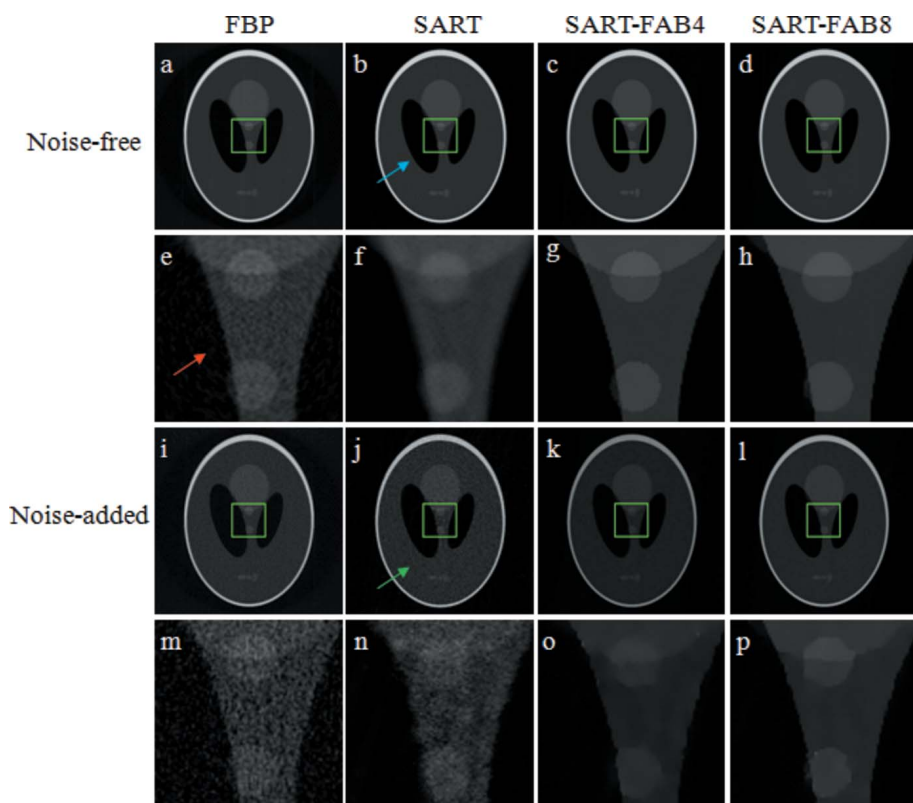


Figure 4 Reconstructed images of the Shepp–Logan phantom using the FBP (a) and (i), SART (b) and (j), SART-FAB4 (c) and (k), and SART-FAB8 (d) and (l) algorithms from noise-free and noisy 60-view projections. Panels (e)–(h) and (m)–(p) are magnified images of the green rectangle regions in panels (a)–(d) and (i)–(l), respectively. The red arrow denotes streak artefacts, the blue arrow denotes oscillating artefacts and the green arrow denotes low-dose noise. The pixel values of the above grey-scale images were normalized to the range [0, 255]. The display window is [0, 180].

4. Real experiment on IL-PCI data

4.1. Data acquisition

An experimental *ex vivo* rat maxilla sample was provided by the Dental Hospital of Tianjin Medical University, and its IL-PCI data were collected at the BL13W1 beamline in SSRF, China. In this experiment, the SDD was 0.8 m, and the energy of the monochromatic beam was set to 33 keV. A charge-coupled device (CCD) camera system with a 36 mm × 5 mm field of view (FOV) was used as the imaging detector, and the effective pixel pitch was 9 μm × 9 μm. The full projection dataset (959-view projections) within a 180° CT scan range was acquired with an exposure time of 10 ms per projection, and the size of the projection image is 3992 × 513 pixels. In addition, ten dark-current images were used to calibrate dark noise in projections while 20 flat-field images were used to calibrate white-field signals in projections (Chen *et al.*, 2012; Baumann, 2014). After phase retrieval using the PAD-BA method, the 192-view projections were evenly chosen from the full projection dataset, and then a sinogram with 192 × 3992 pixels was generated for few-view CT reconstruction of the proposed

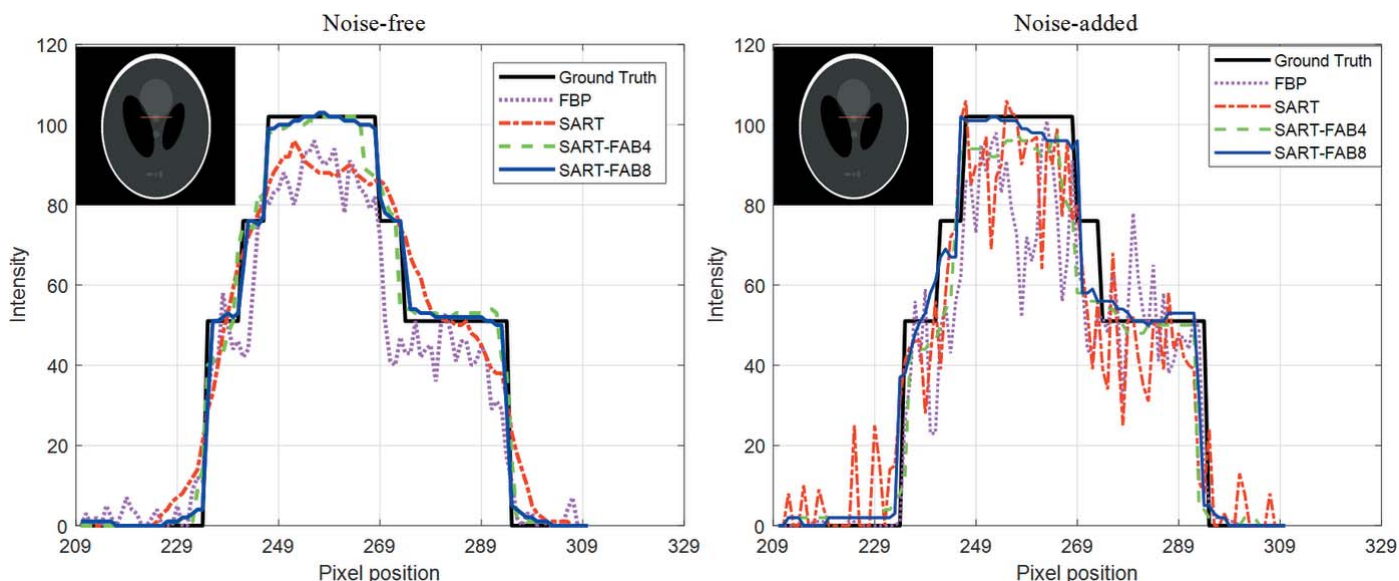


Figure 5 Horizontal profiles of Shepp–Logan phantom images reconstructed using four reconstruction algorithms based on 60-view noise-free projections (left) and 60-view noisy projections (right). The black solid line represents the profile from ground truth; the purple dotted line represents the profile from the FBP algorithm; the red dot-dashed line represents the profile from the SART algorithm; the green dashed line denotes the profile from the SART-FAB4 algorithm; and the blue solid line denotes the profile from the SART-FAB8 algorithm. The profiles were located at the pixel position from the 210th to 310th column and 410th row, as shown in the red line at the upper-left corner of Fig. 5.

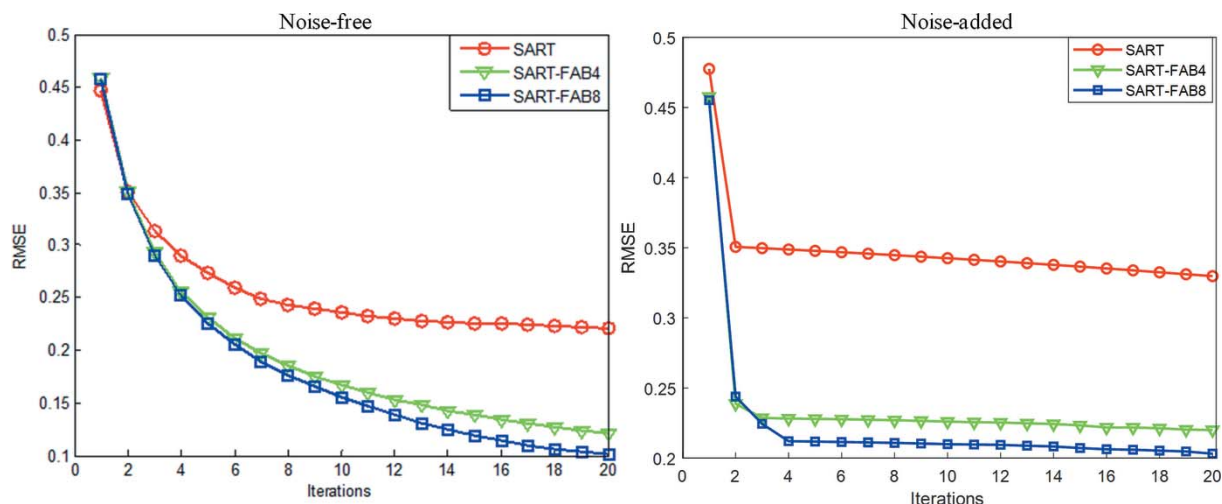


Figure 6 Comparisons of the convergence performance of different iterative reconstruction algorithms based on 60-view noise-free projections (left) and 60-view noisy projections (right). The red line with circles, green line with triangles and blue line with rectangles represent the SART, SART-FAB4 and SART-FAB8 algorithms, respectively.

algorithm. In this work, the missing 767-view projections were compensated by interpolation between the acquired 192-view projections, and then the compensated 959-view projections were used to evaluate the performance of the FBP algorithm in few-view CT reconstruction.

4.2. Experimental results

Fig. 7 depicts reconstructions of the rat maxilla sample using the FBP, SART, SART-FAB4 and SART-FAB8 algorithms. Here, the reconstructed slice of the rat maxilla sample with the full projection dataset using the FBP algorithm is utilized as the reference image, as shown in Fig. 7(a). Fig. 7(b) is a reconstructed slice of rat maxilla sample with the compensated 959-view projections using FBP algorithm, and Figs. 7(c)–7(e) are reconstructed slices of rat maxilla sample with 192-view projections using the SART, SART-FAB4 and SART-FAB8 algorithms, respectively. Fig. 7(b) shows that the slice reconstructed using the FBP algorithm has poor image quality; the textures, fine structures and edges are severely affected by streak artefacts and blur, and the subsequent image analysis (*i.e.* image segmentation, texture analysis and structure measurement) is influenced. Fig. 7(c) indicates that the SART algorithm has the potential to

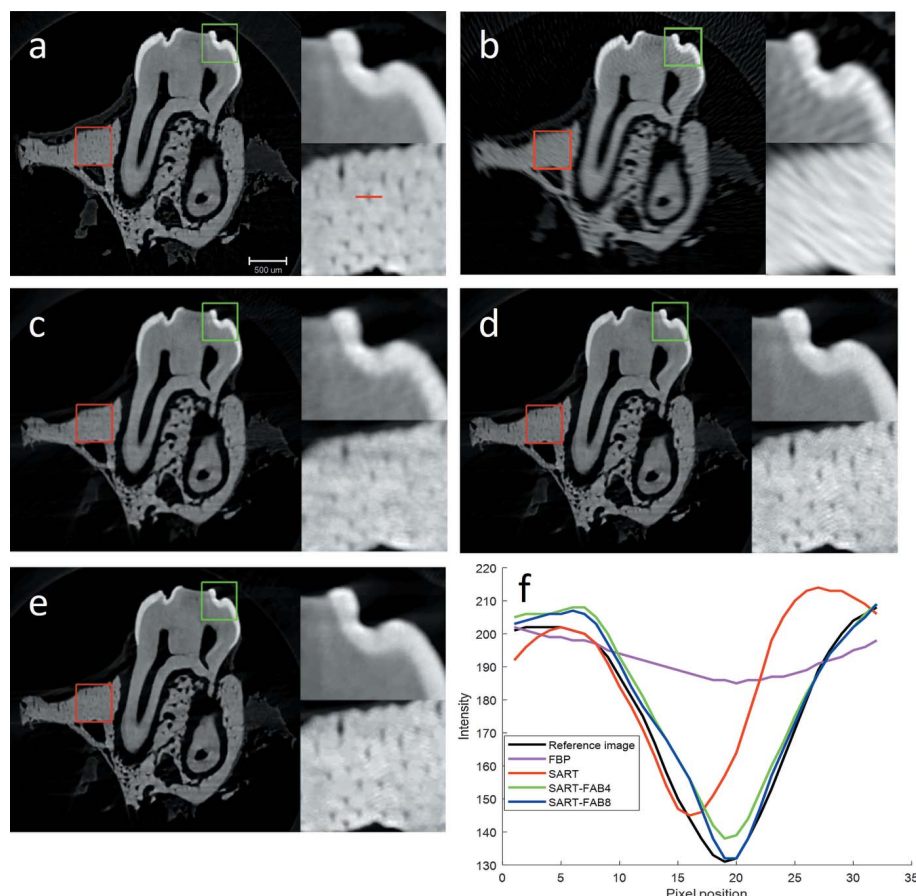


Figure 7 Reconstructed images of rat maxilla sample using four reconstruction algorithms. The image reconstructed from the full projection dataset using the FBP algorithm is chosen as the reference image (a). The image reconstructed with the compensated 959-view projections using FBP (b), and images reconstructed with 192-view projection data using SART (c), SART-FAB4 (d) and SART-FAB8 (e) algorithms are shown. (f) Horizontal profiles of the same position [shown by the red line in (a), which crossed through an alveolar fossa] in (a)–(e). The two right-hand subgraphs in (a)–(e) are magnified images of the green rectangle regions and red rectangle regions in (a)–(e). Pixel values of the above grey-scale images were normalized to the range [0, 255]. The display window is [0, 200].

reduce streak artefacts, but a poor ability to preserve the textures, fine structures and edges using few-view CT reconstruction. From Figs. 7(d)–7(e), it can be seen that the image qualities (e.g. textures, fine structures and edges) have been improved significantly compared with the FBP and SART algorithm, suggesting that the SART-FAB4 and SART-FAB8 algorithms can preserve the textures, fine structures and edges using few-view CT reconstruction. Comparing Figs. 7(d) and 7(e), we can see that the latter has fewer artefacts and clearer detailed features (e.g. textures, structures and edge details), indicating that the SART-FAB8 algorithm yields a better reconstruction result than the SART-FAB4 algorithm.

4.3. Result analysis

To assess the accuracy of four different reconstruction algorithms, the position labelled with the red line in Fig. 7(a), which crossed through the alveolar fossa, was utilized, and the horizontal profiles of the corresponding positions in Figs. 7(a)–7(e) are shown in Fig. 7(f). In Fig. 7(f), it can be seen that the profile and intensity of alveolar fossa using the SART-FAB8 algorithm is closest to the reference image, demonstrating that the accuracy of the SART-FAB8 algorithm is the highest. By comparison, the reconstructed image using the FBP algorithm is the worst; distortions caused by insufficient projection data may impair the analysis and judgement of doctors or researchers, which suggests that the SART-FAB8 algorithm has important value in the case of few-view CT reconstruction. To quantitatively evaluate the reconstruction results of the different methods using the same projection dataset (192-view projections), the UQI, PSNR and RMSE values of the reconstructed images and the computation times of the four reconstruction algorithms are provided in Table 2. As seen from Table 2, when being used to complete the same reconstruction task, the FBP algorithm takes only a few seconds; the SART, SART-FAB4 and SART-FAB8 algorithms require more than 4000 s, and the SART-FAB8 algorithm has the longest computation time. However, the UQI and PSNR values of the SART-FAB8 algorithm are obviously the largest, and, correspondingly, the RMSE value is the smallest. These quantitative results confirmed that the reconstructed image from the SART-FAB8 algorithm has the fewest errors and the best image quality.

5. Discussion and conclusion

In this study, the SART-FAB8 algorithm was proposed for accurate CT reconstruction under the few-view condition. This algorithm was applied to reconstruct the Shepp–Logan phantom and *ex vivo* rat maxilla data obtained by IL-PCI in the case of few-view projections, and the FBP, SART, SART-FAB4 algorithms were adopted as comparison algorithms. The results indicated that the SART-FAB8 algorithm was an effective method of dose reduction for IL-PCCT that could not only reduce streak artefacts and suppress oscillating artefacts but could also preserve textures, fine structures and edge details. Compared with the SART and SART-FAB4

Table 2

Quality metrics of the reconstructed rat maxilla images in Fig. 7.

Method	UQI	PSNR (dB)	RMSE	Time (s)
FBP	0.9357	23.8294	0.7965	6.9828
SART	0.9546	24.1492	0.7463	4042.8
SART-FAB4	0.9735	28.2308	0.6793	4350.9
SART-FAB8	0.9836	29.3457	0.6309	4788.2

algorithms, the SART-FAB8 algorithm had the fastest convergence speed, which may help to address the large-scale computation problem in the practical datasets. With the wide application of IL-PCCT in biological science, it has been demonstrated that IL-PCCT has outstanding potential to reveal detailed microstructures inside biological specimens without injecting contrast agents. In recent years, IL-PCI experiments have been conducted on conventional X-ray sources and demonstrated that comparable image quality could be produced using a benchtop imaging system (Gundogdu *et al.*, 2007; Zysk *et al.*, 2012; Larsson *et al.*, 2016). These findings may pave the way for the realization of preclinical or clinical IL-PCI systems. In principle, IL-PCI can be used for *in vivo* imaging, although many challenges still remain, including the limited field of view, sample motion, high radiation dose and so on (Sztrókay *et al.*, 2012; Bravin & Coan, 2012). In fact, this research is underway. We are currently working to reduce the radiation dose of IL-PCCT while maintaining acceptable image quality using newly optimized CT reconstruction algorithms. Although the performance of our proposed algorithm still requires improvement, e.g. the proposed algorithm has a long computation time, which can be overcome by graphics processing unit (GPU)-based speedup techniques (Tian *et al.*, 2011; Liu *et al.*, 2017), it is worth mentioning that this algorithm was able to reconstruct a high-quality slice of rat maxilla using approximately 20% of the projection data from the full dataset, indicating that this algorithm is a valuable tool for IL-PCCT in low-dose CT reconstruction. In further research, reducing the number of parameters in SART-FAB8 while retaining excellent performance will be an important goal. Moreover, further studies will be performed to assess whether the developed algorithm also applies for *in vivo* data.

Acknowledgements

The authors would like to thank the staff from beamline (BL13W1) of SSRF, China, for their kindly assistance during the experiments.

Funding information

The following funding is acknowledged: The National Natural Science Foundation of China (grant No. 81671683; grant No. 81371549); The Natural Science Foundation of Tianjin City in China (grant No. 16JCYBJC28600); The Science and Technology Commission Foundation of Tianjin (grant No. 2015KZ111); The Open Project of Key laboratory of Opto-electronic Information Technology, Ministry of Education

(grant No. 2017KFKT004); The Foundation of Tianjin university of technology and education (grant No. KJ12-01; grant No. KJ17-36).

References

- Baumann, M. (2014). Master's thesis, pp. 6–12, KTH Royal Institute of Technology, Stockholm, Sweden.
- Bian, Z. Y., Zeng, D., Zhang, Z., Gong, C. F., Tian, X. M., Yan, G., Huang, J., Guo, H., Chen, B., Zhang, J., Feng, Q. J., Chen, W. F. & Ma, J. H. (2017). *Med. Phys.* **44**, e188–e201.
- Brandhuber, M., Armbruster, M., Zupanc, B., Coan, P., Brun, E., Sommer, W. & Rentsch, M. (2016). *Invest. Radiol.* **51**, 170–176.
- Bravin, A. & Coan, P. (2012). *Phys. Med. Biol.* **57**, 2931–2942.
- Bronnikov, A. V. (1999). *Opt. Commun.* **171**, 239–244.
- Bronnikov, A. V. (2002). *J. Opt. Soc. Am. A*, **19**, 472–480.
- Cao, Y., Zhou, Y., Ni, S., Wu, T., Li, P., Liao, S., Hu, J. & Lu, H. (2017). *J. Neurotrauma*, **34**, 1187–1199.
- Chen, R.-C., Dreossi, D., Mancini, L., Menk, R., Rigon, L., Xiao, T.-Q. & Longo, R. (2012). *J. Synchrotron Rad.* **19**, 836–845.
- Chen, R. C., Rigon, L. & Longo, R. (2011). *J. Phys. D Appl. Phys.* **44**, 495401.
- Chen, R. C., Rigon, L. & Longo, R. (2013). *Opt. Express*, **21**, 7384–7399.
- Gerig, G., Kubler, O., Kikinis, R. & Jolesz, F. (1992). *IEEE Trans. Med. Imaging*, **11**, 221–232.
- Gilboa, G., Sochen, N. & Zeevi, Y. (2002). *IEEE Trans. Image Process.* **11**, 689–703.
- Groso, A., Abela, R. & Stampanoni, M. (2006). *Opt. Express*, **14**, 8103–8110.
- Gundogdu, O., Nirgianaki, E., Che Ismail, E., Jenneson, P. M. & Bradley, D. A. (2007). *Appl. Radiat. Isot.* **65**, 1337–1344.
- Gureyev, T. E., Davis, T. J., Pogany, A., Mayo, S. C. & Wilkins, S. W. (2004). *Appl. Opt.* **43**, 2418–2430.
- Hansen, P. & Saxild-Hansen, M. (2012). *J. Comput. Appl. Math.* **236**, 2167–2178.
- Hetterich, H., Webber, N., Willner, M., Herzen, J., Birnbacher, L., Hipp, A., Marschner, M., Auweter, S. D., Habbel, C., Schüller, U., Bamberg, F., Ertl-Wagner, B., Pfeiffer, F. & Saam, T. (2016). *Eur. Radiol.* **26**, 3223–3233.
- Jian, J., Yang, H., Zhao, X., Xuan, R., Zhang, Y., Li, D. & Hu, C. (2016). *J. Synchrotron Rad.* **23**, 600–605.
- Langer, M., Cloetens, P. & Peyrin, F. (2009). *J. Opt. Soc. Am. A*, **26**, 1877–1882.
- Larsson, D. H., Vågberg, W., Yaroshenko, A., Yildirim, A. Ö. & Hertz, H. M. (2016). *Sci. Rep.* **6**, 39074.
- Lee, P. C. (2015). *Opt. Express*, **23**, 10668–10679.
- Liu, R., Kalra, M. K., Hsieh, J. & Yu, H. (2017). *JSM. Biomed. Imaging. Data. Papers*, **4**, 1008.
- Liu, X. X., Zhao, J., Sun, J. Q., Gu, X., Xiao, T. Q., Liu, P. & Xu, L. X. (2010). *Phys. Med. Biol.* **55**, 2399–2409.
- Liu, Y., Ma, J. H., Fan, Y. & Liang, Z. R. (2012). *Phys. Med. Biol.* **57**, 7923–7956.
- Mai, C., Verleden, S. E., McDonough, J. E., Willems, S., De Wever, W., Coolen, J., Dubbeldam, A., Van Raemdonck, D. E., Verbeken, E. K., Verleden, G. M., Hogg, J. C., Vanaudenaerde, B. M., Wuyts, W. A. & Verschakelen, J. A. (2017). *Radiology*, **283**, 252–263.
- Melli, S., Wahid, K., Babyn, P., Montgomery, J., Snead, E., El-Gayed, A., Pettitt, M., Wolkowski, B. & Wesolowski, M. (2016). *Nucl. Instrum. Methods Phys. Res. A*, **806**, 307–317.
- Momose, A., Takeda, T., Itai, Y. & Hirano, K. (1996). *Nat. Med.* **2**, 473–475.
- Nieniewski, M. (2014). *International Conference, ICCVG 2014*, edited by L. J. Chmielewski, R. Kozera, B.-S. Shin and K. Wojciechowski, Vol. 8671 of *Lecture Notes in Computer Science*, pp. 454–461. Heidelberg: Springer.
- Nugent, K. A., Gureyev, T. E., Cookson, D. J., Paganin, D. & Barnea, Z. (1996). *Phys. Rev. Lett.* **77**, 2961–2964.
- Paganin, D., Mayo, S., Gureyev, T., Miller, P. & Wilkins, S. (2002). *J. Microsc.* **206**, 33–40.
- Prasath, V. B., Urbano, J. M. & Vorotnikov, D. (2015). *Inverse Probl.* **31**, 1–30.
- Rastogi, A., Maiwall, R., Bihari, C., Ahuja, A., Kumar, A., Singh, T., Wani, Z. A. & Sarin, S. K. (2013). *Histopathology*, **62**, 731–741.
- Sidky, E. Y., Kao, C.-M. & Pan, X. (2006). *J. X-ray Sci. Technol.* **14**, 119–139.
- Snigirev, A., Snigireva, I., Kohn, V., Kuznetsov, S. & Schelokov, I. (1995). *Rev. Sci. Instrum.* **66**, 5486–5492.
- Stampanoni, M., Wang, Z. T., Thüning, T., David, C., Roessl, E., Trippel, M., Kubik-Huch, R. A., Singer, G., Hohl, M. K. & Hauser, N. (2011). *Invest. Radiol.* **46**, 801–806.
- Sztróky, A., Diemoz, P. C., Schlossbauer, T., Brun, E., Bamberg, F., Mayr, D., Reiser, M. F., Bravin, A. & Coan, P. (2012). *Phys. Med. Biol.* **57**, 2931–2942.
- Tian, Z., Jia, X., Yuan, K. H., Pan, T. S. & Jiang, S. B. (2011). *Phys. Med. Biol.* **56**, 5949–5967.
- Tsiotsios, C. & Petrou, M. (2012). *Pattern Recogn.* **46**, 1369–1381.
- Wang, Z. & Bovik, A. (2002). *IEEE Signal Process. Lett.* **9**, 81–84.
- Weik, M., Gilboa, G. & Weickert, J. (2009). *Scale-Space and Variational Methods in Computer Vision*, edited by X.-C. Tai, K. Mørken, M. Lysaker and K.-A. Lie, Vol. 5567 of *Lecture Notes in Computer Science*, pp. 527–538. Berlin: Springer.
- Wu, X. Z. & Liu, H. (2005). *Opt. Express*, **13**, 6000–6014.
- Xuan, R., Zhao, X., Hu, D., Jian, J., Wang, T. & Hu, C. (2015). *Sci. Rep.* **5**, 11500.
- Yang, X., Hofmann, R., Dapp, R., van de Kamp, T., dos Santos Rolo, T., Xiao, X., Moosmann, J., Kashef, J. & Stotzka, R. (2015). *Opt. Express*, **23**, 5368–5387.
- Zhou, H. C., Zhu, J. B. & Wang, Z. M. (2004). *Chin. J. Electron.* **12**, 2070–2073.
- Zysk, A. M., Garson, A. B., Xu, Q., Brey, E. M., Zhou, W., Brankov, J. G., Wernick, M. N., Kuszak, J. R. & Anastasio, M. A. (2012). *Biomed. Opt. Express*, **3**, 1924–1932.